Supplementary Material: Excitonic effects at the temperature-dependent E_1 and $E_1 + \Delta_1$ critical points of Ge

(*Electronic mail: cobhc14@nmsu.edu.)

(Dated: 1 June 2025)

Carlos A. Armenta* and Stefan Zollner

Department of Physics, New Mexico State University, Las Cruces, NM 88003-8001, USA

S1. EFFECTIVE MASSES

A. Parabolic approximation at the L-point

The E_1 and $E_1 + \Delta_1$ critical points (CPs) presented in Fig. 1b arise from interband transitions taking place from the heavy-hole ($L_4^- \oplus L_5^-$ -band) and light-hole (L_6^- -band) valence band (VB) to the L_6^+ conduction band (CB), respectively. The symmetries associated with these bands correspond to the set of wave function basis vectors^{1,17}

$$L_{6}^{+}: \qquad |Z\uparrow\rangle, |Z\downarrow\rangle,$$

$$L_{4}^{-} \oplus L_{5}^{-}: \qquad \frac{1}{\sqrt{2}}|X+iY\uparrow\rangle, \frac{1}{\sqrt{2}}|X-iY\downarrow\rangle,$$

$$L_{6}^{-}: \qquad \frac{1}{\sqrt{2}}|X+iY\downarrow\rangle, \frac{1}{\sqrt{2}}|X-iY\uparrow\rangle.$$
(S1)

Just like in Sec. II, the *z*-axis was chosen along the Λ -direction. In this basis, and with the aid of $\mathbf{k} \cdot \mathbf{p}$ theory, we can explicitly calculate the matrix $\langle u_{n0} | \mathbf{k} \cdot \mathbf{p} | u_{n'0} \rangle$ to get an expression for the effective masses of the bands (*n* is the index of the band). We note that the only non-zero momentum matrix elements are^{1,17}

$$-i\langle Z|p_x|X\rangle = -i\langle Z|p_Y|Y\rangle = \overline{P}.$$
 (S2)

Naturally, the states in (S1) with opposite spins will not couple. Hence, the 6-band $\mathbf{k} \cdot \mathbf{p}$ Hamiltonian will become a 3×3 matrix represented as follows: 1,17

$$\langle u_{n0} | \mathbf{k} \cdot \mathbf{p} | u_{n'0} \rangle = \begin{bmatrix} \langle L_6^+ | \mathbf{k} \cdot \mathbf{p} | L_6^+ \rangle & \langle L_6^+ | \mathbf{k} \cdot \mathbf{p} | L_4 \rangle & \langle L_6^+ | \mathbf{k} \cdot \mathbf{p} | L_6^- \rangle \\ \langle L_4 | \mathbf{k} \cdot \mathbf{p} | L_6^+ \rangle & \langle L_4 | \mathbf{k} \cdot \mathbf{p} | L_4 \rangle & \langle L_4 | \mathbf{k} \cdot \mathbf{p} | L_6^- \rangle \\ \langle L_6^- | \mathbf{k} \cdot \mathbf{p} | L_6^+ \rangle & \langle L_6^- | \mathbf{k} \cdot \mathbf{p} | L_4 \rangle & \langle L_6^- | \mathbf{k} \cdot \mathbf{p} | L_6^- \rangle \end{bmatrix}$$

$$= \begin{bmatrix} 0 & \frac{i\overline{P}}{\sqrt{2}} k_{\perp} & \frac{i\overline{P}}{\sqrt{2}} k_{\perp} \\ -\frac{i\overline{P}}{\sqrt{2}} k_{\perp} & 0 & 0 \\ -\frac{i\overline{P}}{\sqrt{2}} k_{\perp} & 0 & 0 \end{bmatrix}. \tag{S3}$$

Since the only matrix elements that are nonzero are perpendicular to $|Z\rangle$, the wave vector **k** reduces to k_{\perp} and the motion of the carriers gets restricted to a two-dimensional plane. The full Hamiltonian is given by 1,17

$$\mathcal{H}_{\mathbf{0}} + \tilde{\mathcal{H}}_{\mathbf{k}} = \begin{bmatrix} E_1 & \frac{i\hbar \overline{P}}{m_0 \sqrt{2}} k_{\perp} & \frac{i\hbar \overline{P}}{m_0 \sqrt{2}} k_{\perp} \\ -\frac{i\hbar \overline{P}}{m_0 \sqrt{2}} k_{\perp} & 0 & 0 \\ -\frac{i\hbar \overline{P}}{m_0 \sqrt{2}} k_{\perp} & 0 & -\Delta_1 \end{bmatrix}.$$
(S4)

After diagonalizing the matrix (S4), we get the characteristic equation

$$\tilde{E}^{3} - (E_{1} - \Delta_{1})\tilde{E}^{2} - \left(E_{1}\Delta_{1} + \frac{\hbar^{2}\overline{P}^{2}k_{\perp}^{2}}{m_{0}^{2}}\right)\tilde{E} - \frac{\hbar^{2}\overline{P}^{2}k_{\perp}^{2}\Delta_{1}}{2m_{0}^{2}} = 0,$$
(S5)

where $\tilde{E} = E - \hbar^2 k^2 / 2m_0$ is the modified energy parameter introduced by Kane⁶² (where the kinetic energy of the free electron has been subtracted). For small values of k_{\perp} , we can solve Eq. (S5) perturbatively to get the 3 solutions (one for each band):^{7,51}

$$E_{\text{CB}} = E_1 + \frac{\hbar^2 k_{\perp}^2}{2} \underbrace{\left[\frac{1}{m_0} + \frac{E_P}{m_0} \left(\frac{1}{E_1} + \frac{1}{E_1 + \Delta_1} \right) \right]}_{1/m_1^{(L_6^+)}}$$
(S6)

$$E_{\rm hh} = \frac{\hbar^2 k_{\perp}^2}{2} \underbrace{\left(\frac{1}{m_0} - \frac{E_P}{m_0 E_1}\right)}_{1/m_{\perp}^{(L_4^- \oplus L_5^-)}} \tag{S7}$$

$$E_{\rm lh} = -\Delta_1 + \frac{\hbar^2 k_\perp^2}{2} \left[\frac{1}{m_0} - \frac{E_P}{m_0 (E_1 + \Delta_1)} \right]$$

$$(S8)$$

To simplify the notation, we have made the substitution $E_P = \overline{P}^2/m_0$. Systems of correlated electron-hole pairs generated at the L-point will have a transverse reduced effective mass:¹⁷

$$\mu_{\perp}^{(E_1)} = \left[\frac{1}{m_{\perp}^{(L_0^+)}} - \frac{1}{m_{\perp}^{(L_4^- \oplus L_5^-)}} \right]^{-1} = \left[\frac{E_P}{m_0} \left(\frac{2}{E_1} + \frac{1}{E_1 + \Delta_1} \right) \right]^{-1}$$
 (S9)

and
$$\mu_{\perp}^{(E_1 + \Delta_1)} = \left[\frac{1}{m_{\perp}^{(L_6^+)}} - \frac{1}{m_{\perp}^{(L_6^-)}} \right]^{-1} = \left[\frac{E_P}{m_0} \left(\frac{1}{E_1} + \frac{2}{E_1 + \Delta_1} \right) \right]^{-1}$$
 (S10)

corresponding to the two CPs E_1 and $E_1 + \Delta_1$, respectively.

B. Non-parabolicity at the L-point with small spin-orbit interaction

Instead of approximating for small values of k_{\perp} , we can solve the characteristic Eq. (S5) exactly with Vieta's solution for a cubic equation. These solutions, however, are not useful for our purposes given that they cannot be inverted to get the density of states as a function of energy. Instead, we can use the small spin-orbit (SO) approximation by letting $\Delta_1 \to 0$. If we do this, the characteristic equation becomes

$$\tilde{E}^3 - E_1 \tilde{E}^2 - \frac{\hbar^2 k_{\perp}^2}{m_0} E_P \tilde{E} = 0, \tag{S11}$$

with one solution $\tilde{E}_{hh} = 0$, and the other two

$$\tilde{E}_{\text{CB,lh}} = \frac{E_1 \pm \sqrt{E_1^2 + 4\frac{\hbar^2 k_\perp^2}{m_0} E_P}}{2}.$$
 (S12)

We can expand the square roots in Eq. (S12) in k_{\perp}^2 to obtain

$$E_{\text{CB}} = E_1 + \frac{\hbar^2 k_{\perp}^2}{2m_0} + \frac{E_1}{2} \left(1 + \sqrt{1 + \frac{4\hbar^2 k_{\perp}^2}{m_0} \frac{E_P}{E_1^2}} \right) \approx E_1 + \frac{\hbar^2 k_{\perp}^2}{2m_0} \left(1 + \frac{E_P}{E_1} - \frac{\hbar^2 k_{\perp}^2}{2m_0} \frac{E_P^2}{E_1^3} + 2\frac{\hbar^4 k_{\perp}^4}{2m_0^2} \frac{E_P^3}{E_1^5} \right)$$
(S13)

$$E_{\rm lh} = \frac{\hbar^2 k_{\perp}^2}{2m_0} + \frac{E_1}{2} \left(1 - \sqrt{1 + \frac{4\hbar^2 k_{\perp}^2}{m_0} \frac{E_P}{E_1^2}} \right) \approx \frac{\hbar^2 k_{\perp}^2}{2m_0} \left(1 - \frac{E_P}{E_1} + \frac{\hbar^2 k_{\perp}^2}{2m_0} \frac{E_P^2}{E_1^3} - 2\frac{\hbar^4 k_{\perp}^4}{2m_0^2} \frac{E_P^3}{E_1^5} \right). \tag{S14}$$

FIG. S1 shows the bands of the exact solution, the parabolic, and the small SO approximation. The CB in the small SO approximation is almost identical to the 6-band solution. For the lh-band, the curvature of the small SO approximation is similar

to the exact solution, however, the parabolic approximation is in better agreement to the exact solution. On the other hand, even in the 6-band model solution, the hh-band shows the wrong curvature. The band seems almost flat, indicating a nearly infinite transverse mass. Cardona states that including non-parabolicity terms linear in k_{\perp} make the transverse reduce mass for E_1 infinite.⁵⁴ However, this is in the Λ -region (and not at the L-valley). Unfortunately, this solution does not resemble what we see in $\mathbf{k} \cdot \mathbf{p}$ -theory calculations with higher number of bands.²⁵ Further calculations probing not only the bottom of the L-valley, but also the Λ -direction away from the L-valley are needed.

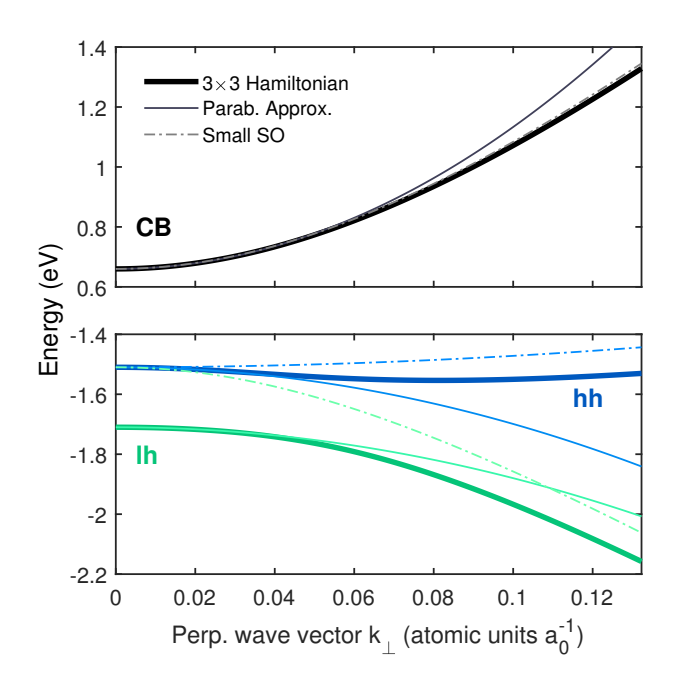


FIG. S1: Band structure of Ge at the L-valley. The perpendicular k_{\perp} -vector is shown in atomic units where $a_0 = 0.53$ Å. The thick solid lines represent the exact solution to the 3×3 Hamiltonian in Eq. (S4), the thin solid lines show the parabolic approximation, and the dot-dashed lines are the small spin-orbit approximation.

S2. DIELECTRIC FUNCTION OF GE

Previous attempts to describe the CPs of interest give the line shape of the DF as a step function 17

$$\varepsilon_2^{(E_1)} = \left(\frac{1}{4\pi\varepsilon_0}\right) \frac{16k_{\text{max}}e^2\overline{P}^2\mu_{\perp}^{(E_1)}}{3m_0^2E^2} H(E_1 - E), \tag{S15a}$$

$$\varepsilon_{2}^{(E_{1}+\Delta_{1})} = \left(\frac{1}{4\pi\varepsilon_{0}}\right) \frac{16k_{\text{max}}e^{2}\overline{P}^{2}\mu_{\perp}^{(E_{1}+\Delta_{1})}}{3m_{0}^{2}E^{2}}H(E_{1}+\Delta_{1}-E), \tag{S15b}$$

where H is the Heaviside step function, k_{max} is the maximum range in the k-axis where transitions take place, and \overline{P} is the average momentum matrix element. The real part ε_1 can be calculated from the expression for ε_2 with a Kramers-Kronig transformation. Alternatively, Humlíček gives the full expression for the DF while adding broadening to Eq. (S15) as 18

$$\varepsilon^{(E_1)}(E) = -\left(\frac{1}{4\pi\varepsilon_0}\right) \frac{16k_{\text{max}}e^2\overline{P}^2\mu_{\perp}^{(E_1)}}{3m_0^2\pi E^2} \ln\left[\frac{2(E_1 - i\Gamma - E)}{E_1 - i\Gamma}\right],\tag{S16a}$$

$$\varepsilon^{(E_1 + \Delta_1)}(E) = -\left(\frac{1}{4\pi\varepsilon_0}\right) \frac{16k_{\text{max}}e^2\overline{P}^2\mu_{\perp}^{(E_1 + \Delta_1)}}{3m_0^2\pi E^2} \ln\left[\frac{2(E_1 + \Delta_1 - i\Gamma - E)}{E_1 + \Delta_1 - i\Gamma}\right]. \tag{S16b}$$

Eqs. (S16) give the DF for uncorrelated electron-hole pairs shown by the blue dashed lines in Fig. 2.

In the following, we briefly describe how to derive Eq. (S15a). We start by computing the amplitude in Eq. (3) for the E_1 CP of Ge from the expression for the imaginary part of the dielectric tensor^{1,63}

$$\varepsilon_{2}(E)^{\mu\nu} = \left(\frac{1}{4\pi\varepsilon_{0}}\right) \frac{4\pi^{2}e^{2}\hbar^{2}}{m_{0}^{2}E^{2}} \sum_{CV} \langle V|p_{\mu}|C\rangle \langle C|p_{\nu}|V\rangle \int \frac{d\mathbf{k}}{4\pi^{3}} \delta(E_{C}(\mathbf{k}) - E_{V}(\mathbf{k}) - \hbar\omega). \tag{S17}$$

Since we are dealing with a cubic system, only the diagonal components of the tensor are non-zero. Therefore, we can replace the dielectric tensor with the dielectric function by averaging the contributing components $\varepsilon_2 = (\varepsilon_{xx} + \varepsilon_{yy} + \varepsilon_{zz})/3$. Moreover, from $\mathbf{k} \cdot \mathbf{p}$ theory, the matrix elements reduce to 17

$$\sum_{CV} \langle V | p_{\mu} | C \rangle \langle C | p_{\nu} | V \rangle = \underbrace{\left| \langle C | P_{x} | V \rangle \right|^{2}}_{\overline{P}^{2}/2} + \underbrace{\left| \langle C | P_{y} | V \rangle \right|^{2}}_{0} + \underbrace{\left| \langle C | P_{z} | V \rangle \right|^{2}}_{0} = \overline{P}^{2}, \tag{S18}$$

hence we can replace the matrix element in Eq. (S17) with the average transition matrix element \overline{P} . Finally, we multiply the DF by 4 to account for the L-valley degeneracy. The result is

$$\varepsilon_2(E) = \left(\frac{1}{4\pi\varepsilon_0}\right) \frac{4\pi^2 e^2 \hbar^2}{m_0^2 E^2} \left(\frac{4\overline{P}^2}{3}\right) \int \frac{d\mathbf{k}}{4\pi^3} \delta(E_{\mathbf{C}}(\mathbf{k}) - E_{\mathbf{V}}(\mathbf{k}) - \hbar\omega). \tag{S19}$$

To solve the integral in Eq. (S19), we replace it with the JDOS in Eq. (2) and switch to cylindrical coordinates. In the new coordinate system, the DF looks like

$$\varepsilon_2(E) = \left(\frac{1}{4\pi\varepsilon_0}\right) \frac{16\pi^2 e^2 \overline{P}^2 \hbar^2}{3m_0^2 E^2} \iiint \frac{k_\rho dk_\rho dk_\phi dk_z}{4\pi^3} \delta\left(E_1 + \frac{\hbar^2 k_\rho^2}{2\mu_\perp} - E\right). \tag{S20}$$

The integral $\int dk_{\varphi} = 2\pi$ is trivial. To integrate over k_{ρ} , we make the substitution $u = \hbar^2 k_{\rho}^2/2\mu_{\perp}$, which transform the integral

$$\int_0^\infty k_\rho dk_\rho \, \delta\left(E_1 + \frac{\hbar^2 k_\rho^2}{2\mu_\perp} - E\right) \to \frac{\mu_\perp}{\hbar^2} \int_0^\infty du \, \delta\left(E_1 + u - E\right). \tag{S21}$$

Its solution yields the Heaviside step function $H(E_1 - E)$. Finally, the integral over k_z needs to be limited to the range where the transitions take place. We call this k_{max} . The final result for E_1 is

$$\varepsilon_2^{(E_1)} = \frac{A}{E^2} H(E_1 - E), \text{ with } A = \frac{4e^2 \overline{P}^2 \mu_{\perp}^{(E_1)}}{3\pi \varepsilon_0 m_0^2} k_{\text{max}},$$
(S22)

which is simply Eq. (S15a). Notice the similarity between the amplitudes in Eq. (S22) and Eq. (4a). These amplitudes are the same if we simply replace the transition matrix element $\mathbf{e} \cdot \mathbf{M}_{CV} \to \overline{P}^2 k_{max}/3$ and multiply by the valley degeneracy (multiply by 4 for L-valley).

S3. UNRENORMALIZED ENERGIES

To get the unrenormalized energies of the CPs, we will follow the procedure by Zollner *et al.*⁴² where they give the unrenormalized value for the direct bandgap E_0 as

$$E_0^u(T) = E_0^u(T = 0 \text{ K}) - 3B \left(\frac{\partial E_0^{\text{exp}}}{\partial p}\right)_T \int_0^T \alpha(\theta) d\theta, \tag{S23}$$

where the superscript u stands for unrenormalized, B is the bulk modulus, $\alpha(T)$ is the temperature-dependent thermal expansion coefficient, and p is the pressure. For our purposes, we will replace the unrenormalized energy at zero temperature with the fitted parameter E_a in the Bose-Einstein model of Eq. (15). The fitted parameters E_a , E_b , and θ_B in Table I are obtained by fitting the experimental CP energies of Table SI. Fig. S2 (b) shows the experimental energy of the E_1 and $E_1 + \Delta_1$ CPs as a function of temperature (dot-dashed lines). To subtract the thermal effect, we use the thermal expansion coefficient given by Eq. (14). Menéndez et al. obtained the values in Eq. (8) by fitting the experimental thermal expansion data from Ma and Tse. ⁴⁰ As

an alternative to Eq. (8), we could also use a more sophisticated expression for the thermal expansion coefficient provided by Roucka *et al.* as⁶⁴

$$\alpha(T) = \frac{4k_{\rm B}}{a_0^3 B} \left[\frac{2}{3} \gamma_{\rm TA} \left(\frac{\Theta_{\rm TA}}{T} \right)^2 \frac{e^{\Theta_{\rm TA}/T}}{\left(e^{\Theta_{\rm TA}/T} - 1 \right)^2} + \gamma_{\rm LA} \left(\frac{T}{\Theta_{\rm LA}} \right)^3 \int_0^{\Theta_{\rm LA}/T} \frac{x^4 e^x}{\left(e^x - 1 \right)^2} dx + \gamma_{\rm opt} \left(\frac{\Theta_{\rm opt}}{T} \right)^2 \frac{e^{\Theta_{\rm opt}/T}}{\left(e^{\Theta_{\rm opt}/T} - 1 \right)^2} \right], \quad (S24)$$

where $a_0 = 5.6568$ Å is the lattice constant, 65 γ is the Grüneisen parameter, and Θ is the Debye temperature. The subscripts LA, TA, and opt stand for the longitudinal acoustic, transverse acoustic, and optical modes, respectively. As seen in Fig. S2 (a), the more complicated expression in Eq. (S24) yields an almost identical result to Eq. (14). Therefore, we settle on using Eq. (8) for this work. Fig. S2 (a) also shows experimental thermal expansion coefficients from the literature. 66,67

The result of the unrenormalized energy in Eq. (S23) is shown in Fig. S2 (b) (solid lines). For this calculation, we take the value of $(\partial E_1/\partial p)_T \approx [\partial (E_1+\Delta_1)/\partial p]_T$. We justify this assumption by noting that the SO shift Δ_1 is related to atomic effects and it is, for the most part, unaffected by the distance of the atoms within the lattice. Finally, Fig. S2 (c) shows the exciton binding energies for both CPs in the left axis (solid lines), as well as the reduced masses on the right axis (dashed lines).

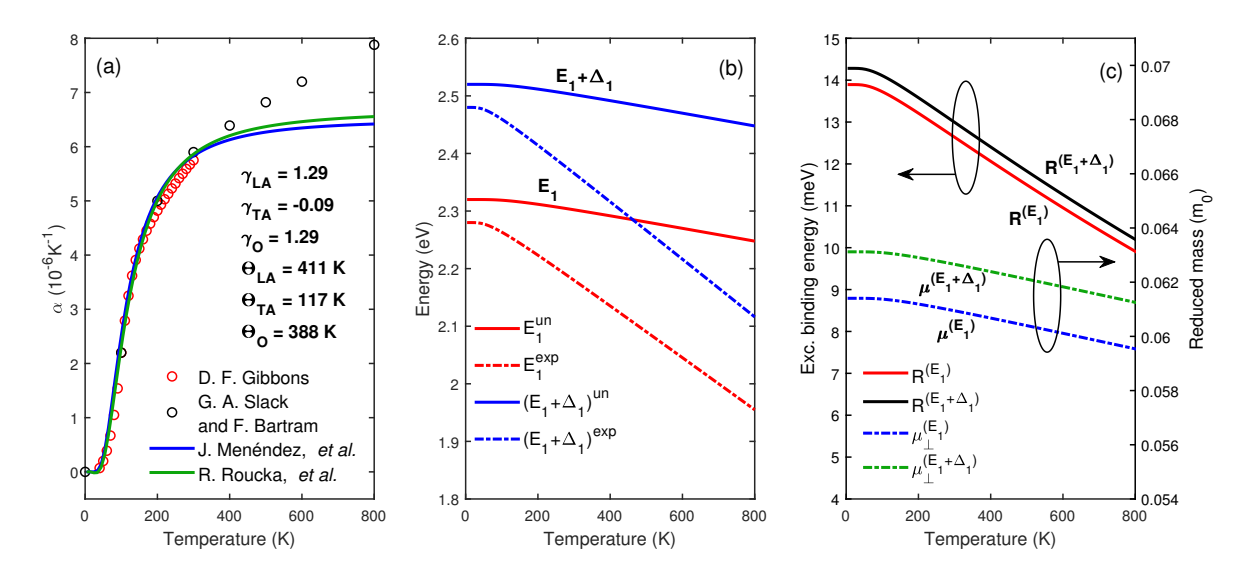


FIG. S2: (a) Thermal expansion coefficient from Eq. $(14)^{36}$ (blue solid line) and Eq. $(S24)^{64}$ (green solid line) compared to experimental data (\bigcirc) . 66,67 (b) The experimental values for E_1 and $E_1 + \Delta_1$ (blue and red dot-dashed line, respectively) are shown along with their respective unrenormalized energy (red and blue solid lines, respectively). (c) On the left axis is the binding energy of the excitons of the critical points (black and red solid lines). On the right axis is the transverse reduced effective masses (green and blue dot-dashed lines).

S4. FITTING PROCEDURE

To suppress the noise of the experimental data, we used a direct space convolution of the experimental DF with a digital filter. The convolution \overline{f} between f(x) and b(x) has the following property:

$$\overline{f}(x) = \int_{-\infty}^{\infty} \mathrm{d}x' f(x - x') b(x') = \int_{-\infty}^{\infty} \mathrm{d}x' f(x') b(x - x'). \tag{S25}$$

Note that, in light of Eq. (S25), operations such as $d\overline{f}(x)/dx$ produce the same outcome whether they act on f(x-x') or b(x-x'). To compute the second derivative of the experimental data, we take full advantage of this property by differentiating the digital filter (an analytical function) instead of the experimental data (a set of discrete points). To perform the convolution, we used MATLAB's built-in function conv(u,v), where u and v are the vectors being convoluted. For the fitting procedure, we created a residual vector function with five free parameters $[E_1, \Delta_1, \Gamma^{(E_1)}, \Gamma^{(E_1+\Delta_1)}]$, and ε_{off} . The two components of this vector function consisted of the real and imaginary part of the experimental 2^{nd} derivative of the DF minus the corresponding parts of

TABLE SI: Value of the fitting parameters and filter width ΔE for the extended Gauss digital filter. The step size selected was 1 meV from 1.0 to 3.2 eV (2201 points). (f) indicates a fixed parameter.

T	ΔE (meV)	<i>E</i> ₁ (eV)	$E_1 + \Delta_1 \text{ (eV)}$	$\Gamma^{(E_1)}$ (meV)	$\Gamma^{(E_1+\Delta_1)}$ (meV)	$arepsilon_{ m off}$
4 K	12.0	2.2793 ± 0.0009	2.4779 ± 0.002	75 ± 1	96±2	6(f)
100 K	14.5	2.2599 ± 0.0008	2.4600 ± 0.002	79 ± 1	103 ± 2	6(f)
200 K	17.5	2.2187 ± 0.0009	2.4176 ± 0.002	89 ± 1	119 ± 2	7(f)
300 K	21.5	2.1674 ± 0.0009	2.3638 ± 0.002	101 ± 1	136 ± 2	7(f)
400 K	27.5	2.1167 ± 0.0006	2.3147 ± 0.002	115 ± 1	157 ± 2	8(f)
500 K	27.5	2.0656 ± 0.0007	2.2642 ± 0.003	128 ± 1	175 ± 2	8(f)
600 K	25.0	2.0172 ± 0.0009	2.2170 ± 0.003	142 ± 1	193 ± 3	8(f)
700 K	33.0	1.968 ± 0.001	2.1683 ± 0.004	155 ± 1	212 ± 4	8(f)
800 K	35.0	1.917 ± 0.002	2.1182 ± 0.006	171 ± 2	243 ± 6	9(f)

TABLE SII: Value of the fitting parameters and order of polynomial n for the Savitzky-Golay digital filter. The frame length was constrain to 5% of the number of points (11 points). (f) indicates a fixed parameter.

T	n	<i>E</i> ₁ (eV)	$E_1 + \Delta_1 \text{ (eV)}$	$\Gamma^{(E_1)}$ (meV)	$\Gamma^{(E_1+\Delta_1)}$ (meV)	$\epsilon_{ m off}$
4 K	7	2.279 ± 0.002	2.478 ± 0.006	76 ± 3	96±6	6(f)
100 K	7	2.260 ± 0.002	2.460 ± 0.006	80 ± 2	103 ± 5	6(f)
200 K	7	2.219 ± 0.003	2.418 ± 0.005	89 ± 3	119 ± 7	7(f)
300 K	5	2.167 ± 0.003	2.364 ± 0.005	102 ± 2	137 ± 5	7(f)
400 K	5	2.117 ± 0.002	2.315 ± 0.005	116 ± 2	157 ± 6	8(f)
500 K	5	2.066 ± 0.002	2.264 ± 0.007	129 ± 2	175 ± 6	8(f)
600 K	4	2.017 ± 0.002	2.217 ± 0.008	142 ± 3	193 ± 9	8(f)
700 K	3	1.968 ± 0.003	2.17 ± 0.01	155 ± 3	212 ± 12	8(f)
800 K	3	1.917 ± 0.006	2.12 ± 0.02	171 ± 6	234 ± 18	9(f)

the numerical derivative of the model:

$$\operatorname{residual}(E_{1}, \Delta_{1}, \Gamma^{(E_{1})}, \Gamma^{(E_{1} + \Delta_{1})}, \boldsymbol{\varepsilon}_{\operatorname{off}}, E) = \begin{bmatrix} \operatorname{Re}\left\{\frac{\mathrm{d}^{2} \varepsilon^{\exp}(E)}{\mathrm{d}E^{2}}\right\} - \operatorname{Re}\left\{\frac{\mathrm{d}^{2} \varepsilon^{\operatorname{model}}(E_{1}, \Delta_{1}, \Gamma^{(E_{1})}, \Gamma^{(E_{1} + \Delta_{1})}, \boldsymbol{\varepsilon}_{\operatorname{off}}, E)}{\mathrm{d}E^{2}}\right\} \\ - \operatorname{Im}\left\{\frac{\mathrm{d}^{2} \varepsilon^{\exp}(E)}{\mathrm{d}E^{2}}\right\} - \operatorname{Im}\left\{\frac{\mathrm{d}^{2} \varepsilon^{\operatorname{model}}(E_{1}, \Delta_{1}, \Gamma^{(E_{1})}, \Gamma^{(E_{1} + \Delta_{1})}, \boldsymbol{\varepsilon}_{\operatorname{off}}, E)}{\mathrm{d}E^{2}}\right\} \end{bmatrix}. \tag{S26}$$

After creating the residual vector function (S26), we minimized it with the MATLAB function lsqnonlin(fun,x0,lb,ub), where the input fun is the function to be minimized, x0 is the vector with the initial guess for the fitting parameters, lb, and ub are the vectors with the lower and upper bounds for the fitting parameters, respectively.

A. Extended Gaussian digital filter

The extended Gaussian (EG) digital filter of Eq. (18) for M = 4 has the form 46,47

$$b_4(x) = \frac{1}{12288\Delta E\sqrt{\pi}} \left(15120 - \frac{10080x^2}{\Delta E^2} + \frac{1512x^4}{\Delta E^4} - \frac{72x^6}{\Delta E^6} + \frac{x^8}{\Delta E^8} \right) \exp\left(-\frac{x^2}{4\Delta E^2}\right). \tag{S27}$$

However, since we are interested in the 2^{nd} derivative of the data, we can compute the second derivative of Eq. (S27) and perform the convolution with $\varepsilon^{\exp}(E)$ afterward.

$$\frac{\mathrm{d}^2 b_4(x)}{\mathrm{d} x^2} = \frac{1}{49152 \Delta E^3 \sqrt{\pi}} \left(-110880 + \frac{188496 x^2}{\Delta E^2} - \frac{45936 x^4}{\Delta E^4} + \frac{3608 x^6}{\Delta E^6} - \frac{106 x^8}{\Delta E^8} + \frac{x^{10}}{\Delta E^{10}} \right) \exp\left(-\frac{x^2}{4 \Delta E^2} \right). \tag{S28}$$

To select the filter width ΔE , we Fourier-transform the experimental data and plot the natural logarithm of the amplitude C_n of the coefficients as seen Fig. S3 (a). We then eliminate the higher order coefficients (noise) and retain the lower ones which preserve the information of the original signal. The same cutoff of the coefficients is also applied to the Fourier transform of the EG filter $B_4(n)$, shown in Fig. S3 (a) as well. In this figure, we show the Fourier coefficients of the experimental data as a function of the order of coefficients n at 200 K, along with the Fourier transform of the extended Gaussian filter $B_4(n)$ for two different filter widths. For this particular measurement, we selected the cutoff at the 31^{st} coefficient. The reader might find this

cutoff too conservative and that such a large filter width could suppress a portion of the signal. To address these concerns, we repeated the fitting procedure with the cutoff at the 41st coefficient [see the cyan dash-dotted line in Fig. S3 (a)]. We find that including higher-order coefficients increases noise but does not change the fitted energy and broadening parameters beyond their uncertainty. Therefore, we settled with the larger filter width. The dark circles in Fig. S3 (b) show the EG derivatives for this measurement. One of the advantages of this method is the increase in the number of points available in the derivative. In our case, the EG filter produces 2201 derivative points, resulting from the chosen energy step size of 1 meV over the range from 1.0 to 3.2 eV. This is in contrast to the Savitsky-Golay (SG) derivative [shown by the red and blue lines in Fig. S3 (b)], where the derivative is limited to the number of points of the original signal. Once the filter width has been selected, we can minimize the residual function in Eq. (S26) to fit the energy and broadening parameters. Table SI shows the fitted parameters for this method.

B. Savitzky-Golay digital filter

To obtain the SG digital filter, we employed the built-in MATLAB function sgolay(m,fl). This function gives a matrix of a finite impulse response smoothing filter. The input m is the polynomial order and fl is the frame length. We used 11 points for the frame length, which is approximately 5% of the total number of data points (this number must be odd). The order of the polynomial is listed in Table SII for each temperature series. Once we have generated the SG filter, we can obtain the n^{th} derivative by convolving the experimental data with the $(n+1)^{th}$ column of the filter matrix. The solid lines in Fig. S3 (b) show the SG derivatives for the experimental data at 200 K. Table SII shows the final values of the fitted parameters with the SG filter. Notice the similarity of the fitted values for energy and broadening between the two filters.

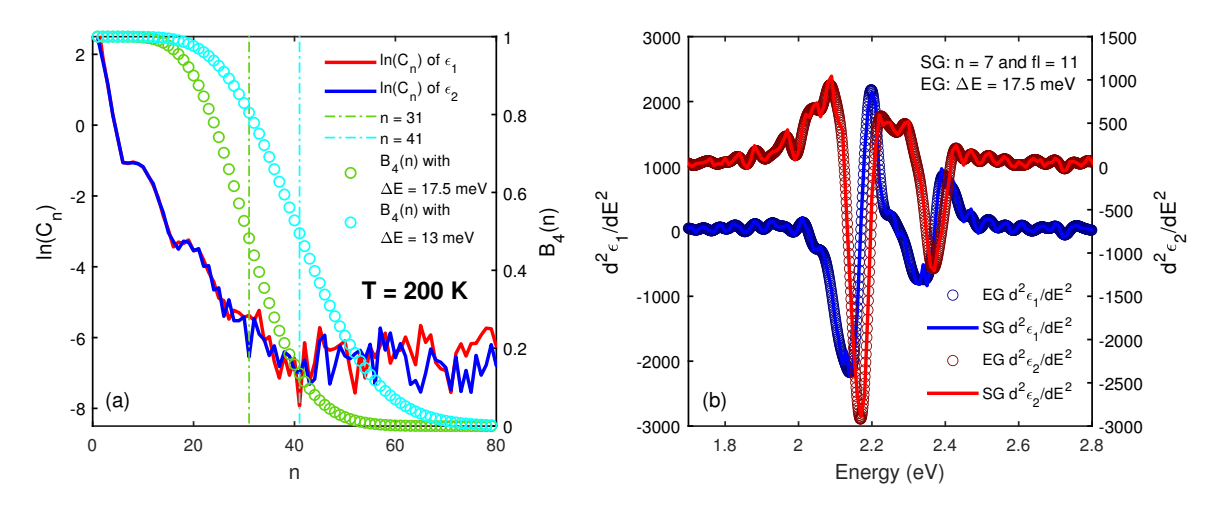


FIG. S3: (a) Natural logarithm of the Fourier coefficient amplitude C_n of the real (red) and imaginary (blue) parts of the dielectric function at 200 K. The same plot also shows the Fourier transform of the extended Gaussian filter (\bigcirc) for different filter widths. (b) 2^{nd} derivative of the dielectric function calculated with the extended Gauss filter (\bigcirc) and with the Savitzky-Golay filter (solid).

S5. DIRECT BANDGAP

The lineshape of the E_0 CP was presented previously by Emminger et al. as⁶

$$\varepsilon(E) = \frac{A\sqrt{R}}{\pi(E + i\Gamma)^2} \left\{ \tilde{g} \left[\xi(E + i\Gamma) \right] + \tilde{g} \left[\xi(-E - i\Gamma) \right] - 2\tilde{g} \left[\xi(0) \right] \right\}, \tag{S29}$$
with $\tilde{g}(\xi) = -2\psi \left(\frac{g}{\xi} \right) - \frac{\xi}{g} - 2\psi (1 - \xi) - \frac{1}{\xi}, \ \xi(z) = \frac{2}{\sqrt{\frac{E_0 - z}{R}} + \sqrt{\frac{E_0 - z}{R}} + \frac{4}{g}}, \text{ and } A = \frac{e^2 \sqrt{m_0}}{\sqrt{2}\pi\varepsilon_0 \hbar^2} \mu_h^{3/2} \frac{E_P}{3}.$

This model is quite similar to Eq. (3), since it also takes into account excitonic (and screening) contributions to the CP. We can improve Eq. (S29) by including non-parabolicity contributions to the effective mass at the Γ -point. By following the procedure in Ref. 42 we use the small spin-orbit (SO) coupling approximation to get an analytical expression for the CB effective mass

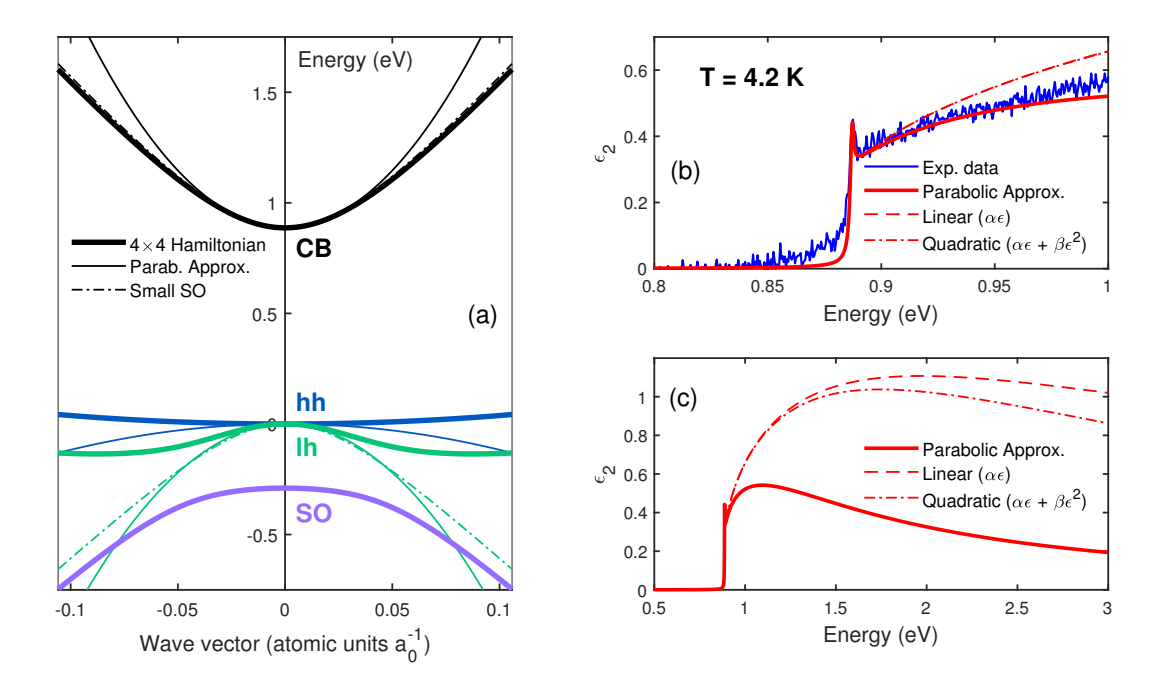


FIG. S4: (a) In addition to the parabolic approximation (thin solid line), we show the exact solution (thick solid line) and the small spin-orbit approximation (dot-dashed) to the 8-band model of the band structure of Ge. (b) Imaginary part of the dielectric function at 4 K in the parabolic approximation (solid) and including non-parabolicity linear terms in $\alpha\varepsilon$ (dashed) and quadratic terms in $\beta\varepsilon^2$ (dot-dashed) of the density of states mass. (c) Parabolic (solid) and non-parabolic (dashed, dot-dashed) models extended up to 3 eV.

and, therefore, the electron density of states (DOS) mass. If we consider an 8-band model (CB, hh, lh, and SO band), our $\mathbf{k} \cdot \mathbf{p}$ Hamiltonian looks like⁶²

$$\mathcal{H}_0 + \tilde{\mathcal{H}}_{\mathbf{k}} = \begin{bmatrix} E_0 & 0 & -\frac{\hbar k}{m_0} iP & 0\\ 0 & -\frac{2\Delta_0}{3} & \frac{2\Delta_0}{3} & 0\\ \frac{\hbar k}{m_0} iP & \frac{2\Delta_0}{3} & -\frac{2\Delta_0}{3} & 0\\ 0 & 0 & 0 & 0 \end{bmatrix}.$$
 (S30)

We can construct an exact solution of the band energies by solving the characteristic equation to this eigenvalue problem. Similar to Eq. (S5), the exact solutions to Eq. (S30) are not useful for our purposes because they cannot be inverted to get the DOS as a function of energy. Instead, we assume that the spin-orbit (SO) coupling is small and approximate $\Delta_0 \to 0$. As a result, this approximation makes the center terms in the Hamiltonian matrix (S30) zero and gives two degenerate solutions of zero (the hh-and SO-band) and two non-zero solutions (the CB and lh-band). In Fig. S4 (a), we can see that in the small SO approximation, the CB fits reasonable well to the exact solution of the band structure (at least in our 8-band 4×4 Hamiltonian model). Since there are two zero solutions in the small SO approximation, the hh- and SO-VB are degenerate and lie on top of the exact solution of the hh-band. The effective mass of the electron in CB and the hole in the lh-band are, therefore, given as

$$m_e = \frac{E_0}{E_P + E_0},$$
 $m_{\text{lh}} = \frac{E_0}{E_P - E_0}.$

However, the band structure in Fig. S4 (a) clearly shows that the small SO approximation does not present a good match with the exact solution of the lh-band. For this reason, we will only consider non-parabolicity effects in the CB, while leaving the VB in its parabolic approximation form. Hence, we will only consider m_e to calculate the DOS mass⁴²

$$m_{e,\text{DOS}} = m_e \left[(1 + \alpha_e \varepsilon + \beta_e \varepsilon^2) (1 + 2\alpha_e \varepsilon + 3\beta_e \varepsilon^2)^2 \right]^{1/3}, \tag{S31}$$

where⁴²

$$\alpha_e = \frac{E_P^2}{E_0(E_0 + E_P)^2},$$

$$\beta_e = -\frac{2E_P^3}{E_0(E_0 + E_P)^4},$$
(S32)

and ε is the energy above the band minimum E_0 . Including α and β into the DOS effective mass has the effect of overestimating ε_2 . This can be seen in Fig. S4 (b). To compensate this, we would have to consider the k-dependence of the matrix element E_P , which should bring ε_2 closer to the experimental value (we do not pursue this here). Still, independently of the approximation, the amplitude of ε_2 is around one between 1.5 and 3 eV. Therefore, including E_0 in the Tanguy line-shape would not be enough to match the experimental data in the E_1 and $E_1 + \Delta_1$ region.

S6. SURFACE EFFECTS

To showcase the dielectric function for different surface orientations, we measured Ge substrates with (100), (110), and (111) surface orientations. We then follow the procedure explained in Sec. III to remove the effects of the oxide layer from the data. The (110) surface orientation had an estimated oxide layer thickness of about 28 Å, whereas the (100) and (111) surfaces had a similar oxide layer thickness of about 25 Å. The resulting point-by-point fits are shown in Fig. S5. It can be seen that the difference between the samples is negligible. Therefore, we find it unlikely that these surface-related effects are responsible for the discrepancies between theory and experiment observed in our model for the dielectric function near the E_1 and $E_1 + \Delta_1$ CPs.

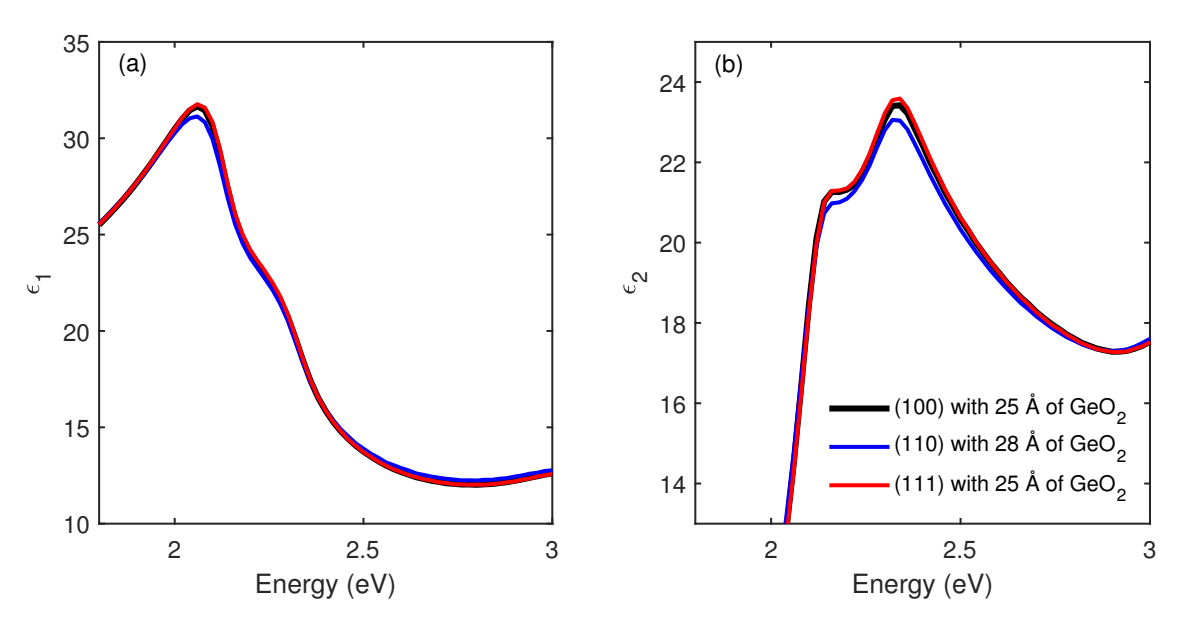


FIG. S5: Real (a) and imaginary (b) parts of the dielectric function of Ge from a point-by-point fit for three substrates with (100), (110), and (111) surface orientations (black, blue, and red, respectively).

ADDITIONAL REFERENCES

⁶² E. O. Kane, J. Phys. Chem. Solids **1**, 249 (1957).

⁶³ H. Kalt and C. F. Klingshirn, Semiconductor Optics 1: Linear Optical Properties of Semiconductors (Springer Nature Switzerland AG, 2019).

⁶⁴ R. Roucka, Y.-Y. Fang, J. Kouvetakis, A. V. G. Chizmeshya, and J. Menéndez, Phys. Rev. B **81** 245214 (2010).

⁶⁵ O. Madelung, *Semiconductors*, Landolt-Börnstein, New Series Vol. 41, Pt. A (Springer-Verlag, Berlin, New York, 2001).

⁶⁶ D. F. Gibbons, Phys. Rev. **112** 136 (1958).

⁶⁷ G. A. Slack, S. F. Bartram, J. Appl. Phys. **46**, 89 (1975).